



# Estimating state of charge and health of lithium-ion batteries with guided waves using built-in piezoelectric sensors/actuators

Purim Ladpli<sup>a,\*</sup>, Fotis Kopsaftopoulos<sup>b</sup>, Fu-Kuo Chang<sup>a</sup>

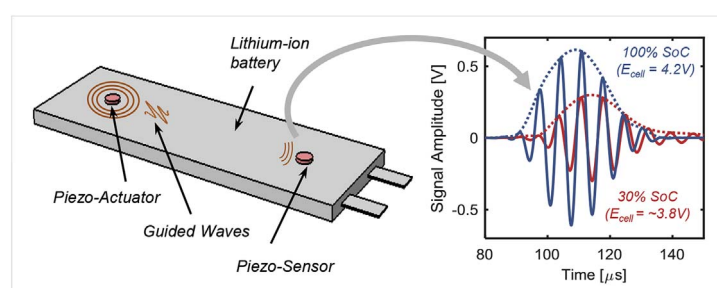
<sup>a</sup> Department of Aeronautics and Astronautics, Stanford University, Stanford, CA, USA

<sup>b</sup> Department of Mechanical, Aerospace and Nuclear Engineering, Rensselaer Polytechnic Institute, Troy, NY, USA

## HIGHLIGHTS

- Guided waves precisely estimate a lithium-ion battery's state of charge and health.
- A simple implementation involves low-profile, built-in piezoelectric transducers.
- Time of flight and signal amplitude are indicative of state of charge and health.
- Signals from multiple propagation paths simplify computation and enhance accuracy.
- Analytical results relate acoustic signature with changes in modulus and density.

## GRAPHICAL ABSTRACT



## ARTICLE INFO

### Keywords:

Lithium-ion battery  
Ultrasonic guided waves  
State of charge  
State of health

## ABSTRACT

This work presents the feasibility of monitoring state of charge (SoC) and state of health (SoH) of lithium-ion pouch batteries with acousto-ultrasonic guided waves. The guided waves are propagated and sensed using low-profile, built-in piezoelectric disc transducers that can be retrofitted onto off-the-shelf batteries. Both experimental and analytical studies are performed to understand the relationship between guided waves generated in a pitch-catch mode and battery SoC/SoH. The preliminary experiments on representative pouch cells show that the changes in time of flight (ToF) and signal amplitude (SA) resulting from shifts in the guided wave signals correlate strongly with the electrochemical charge-discharge cycling and aging. An analytical acoustic model is developed to simulate the variations in electrode moduli and densities during cycling, which correctly validates the absolute values and range of experimental ToF. It is further illustrated via a statistical study that ToF and SA can be used in a prediction model to accurately estimate SoC/SoH. Additionally, by using multiple sensors in a network configuration on the same battery, a significantly more reliable and accurate SoC/SoH prediction is achieved. The indicative results from this study can be extended to develop a unified guided-wave-based framework for SoC/SoH monitoring of many lithium-ion battery applications.

## 1. Introduction

In response to the ever-growing demand for electrical systems, recent extensive battery research, particularly research involving lithium-

ion (Li-ion) batteries, is trying to push the envelope of high-energy battery packs from electric automotive applications to renewable energy storage [1,2]. However, Li-ion batteries are extremely complex systems with a very narrow operating range and are prone to premature

\* Corresponding author. Durand Building, Room 054, 496 Lomita Mall, Stanford University, Stanford, CA 94305, USA.  
E-mail address: [pladpli@stanford.edu](mailto:pladpli@stanford.edu) (P. Ladpli).

unexpected failure [3–5]. To optimize battery performance, lifespan, and most importantly, safety, a battery management system (BMS) is required to perform battery condition monitoring, charge/discharge control, thermal management, cell balancing, and fault mitigation [4–10]. To facilitate the foregoing functions, the BMS must first and foremost be able to accurately monitor the batteries' critical internal states, which primarily include state of charge (SoC) (the charge remaining in the battery with respect to the fully charged capacity, or the equivalent of a fuel gauge) and state of health (SoH) (a degree of degradation in battery health which usually manifests as a reduction in capacity retention) [4–11]. It is a true detriment to the field that the practical implementation of high-energy battery systems is still extremely challenging owing to the lack of a field-deployable, yet affordable battery management system (BMS) that can reliably and accurately monitor SoC/SoH [4–10].

In a laboratory setting, in-situ techniques (e.g., X-ray diffraction [12–14], neutron imaging [15,16], and electrochemical impedance spectroscopy (EIS) [17,18]) can be used to directly probe the physical states of the battery. However, such techniques cannot be practically implemented and, in most cases, can only be performed on small-scale, non-standard cells. In addition, the benefits of having these elaborate electrochemical tools on-board do not justify the significant additional cost and complexity. As it stands, conventional on-board BMSs are therefore limited to the measurement of extrinsic parameters, including voltage, current, and temperature. From these, SoC/SoH are merely approximated using a combination of time-series techniques, battery modelling, parameter identification, and state estimation algorithms [4–10]. In its most rudimentary form, interpolation and time-history integration of on-board collected data are utilized in the form of SoC-OCV lookup and coulomb counting [19]. Other strategies rely on mathematical models of battery dynamics (electrochemical models) [20] or an approximate form of which, commonly referred to as equivalent circuit models [21]. State estimation algorithms, parameter observer, and more advanced signal processing techniques (e.g. Kalman filtering [22], partial differential equation observer [20,23], etc.) are then used in conjunction with these models to estimate SoC/SoH. More recent machine learning and statistical methods (e.g. neural networks [24], support vector machines [23], etc.) have also been incorporated into the model-based methods. Alternately, these are formulated into a model-free, data-driven scheme, which directly exploits the voltage and current measurements or their extracted features (e.g. sample entropy [6,11], incremental capacity analysis [25–28], etc.).

The current techniques have not come to exploit the fact that a Li-ion battery is fundamentally a composite material system. A battery undergoes mechanical evolution, most notably modulus and density distribution, during electrical cycling and aging [3]. Thus, the mechano-electrochemical coupling presents an opportunity for mechanical characterization and inspection techniques to be used to monitor the electrochemical processes. Ultrasonic inspection is one of the most elegant and widely-used solutions in the context of ultrasonic non-destructive evaluation (NDE) [29] and structural health monitoring (SHM) [30,31]. Mechanical stress waves are excited, propagated, and received in a structure, allowing the mechanical properties, structural integrity, and internal damage to be accurately and continuously monitored almost in real time. Ultrasonic inspection can therefore potentially be used to monitor the battery modulus and density activities, and ultimately to estimate the SoC/SoH.

Recent research has utilized ultrasound to probe Li-ion batteries. The work by Sood et al. is one of the pioneering studies to adopt an ultrasonic NDE technique for battery monitoring [32]. In this work, an ultrasonic pulser and a receiver are used to generate through-thickness compressional waves to detect local degradation at the interfaces between electrode layers. The information is then used to qualitatively determine any detrimental delamination of the electrode. Hsieh and Bhadra et al. perform a very comprehensive study using a similar experimental setup on numerous types of commercial batteries [33,34].

Through-thickness bulk-wave transmission and reflection data show correlations with the charge, discharge, and aging processes. The authors also attempt to validate the experimental findings analytically; however, owing to limitations of their model, only the relative changes in wave propagation times are presented. A follow-up work by Davies et al. shows that the propagation time and intensity of the through-thickness bulk waves can be used as predictors for SoC/SoH estimation [35].

Gold et al. introduce the use of a piezoelectric disc transducer pair mounted on the surface of a Li-ion battery using an adhesive, instead of a temporary gel couplant, which provides significantly cleaner signals and prevents baseline variability [36]. Ultrasonic waves are propagated in the form of a modulated sinusoid, as an alternative to a rudimentary ping. The study is limited to discontinuous, incomplete trends of signal parameters at several points during the charge and discharge processes. Gold et al. validate the experimental results analytically with a novel approach that considers the variation in electrode porosities during cycling, despite the numerous assumptions involved.

Most importantly, however, all these previous studies rely on the propagation of through-thickness compressional waves, which usually need external bulky ultrasonic probes and equipment, require extensive operator intervention, and suffer from inaccurate baseline collection [37,38]. In stark contrast, acousto-ultrasonic guided waves take advantage of the geometric boundaries of the structure to 'guide' the wave propagation [31,39]. This allows the stress waves to propagate a long distance in structures of various dimensions and complexities with minimal loss in energy. The complete process can be achieved using an onboard, built-in network of sensors and actuators. Unlike other stress wave counterparts, the properties of guided wave propagation enable a single actuator-sensor pair to have a large coverage area, hence resulting in simultaneous global and local inspection with a minimal footprint [31]. The literature so far has not explored the concept of SoC/SoH estimation with guided waves using a built-in network of piezoelectric transducers, despite its immense potential.

Therefore, the objective of this investigation is to develop a built-in acousto-ultrasonic guided wave technique to monitor SoC/SoH of Li-ion batteries. Building upon our previous companion work [40,41], the cornerstone of this method is the field-deployable use of small-footprint, built-in piezoelectric transducers to propagate windowed tone-burst guided waves. Since guided waves perform best in elongated, plate-like structures [31,39], they are well-suited for the form factor of pouch and prismatic batteries, which are commonly used in electrical systems, from stationary grids to electric vehicles and satellites.

Following is an outline of the rest of the article. Section 2 briefly describes the problem formulation, scope, and constraints. The overall approach to the problem is summarized in Section 3. Sections 4 and 5 present the experimental setup and details of the analytical wave propagation model, respectively. The results from the experiments are fully discussed in Section 6 and compared with findings from the analytical model. Section 7 constitutes a statistical framework that predicts battery SoC/SoH using guided wave features, followed by conclusions in Section 8.

## 2. Problem statement

Consider a Li-ion pouch cell, as shown in Fig. 1, which is equipped with permanently mounted piezoelectric disc transducers which can serve as actuators and sensors. One of the piezoelectric discs can be chosen as an actuator to generate acousto-ultrasonic guided waves. The other piezoelectric disc then serves as a receiver to record the transmitted guided wave signals. It is desired to correlate the guided wave signals from piezoelectric sensors with battery SoC/SoH through both experiments and analysis. The obtained results are imperative for evaluating the efficacy of SoC/SoH prediction using guided waves with built-in sensors/actuators. The proposed technique is to be evaluated on indicative commercial Li-ion pouch cells (graphite/NMC chemistry;

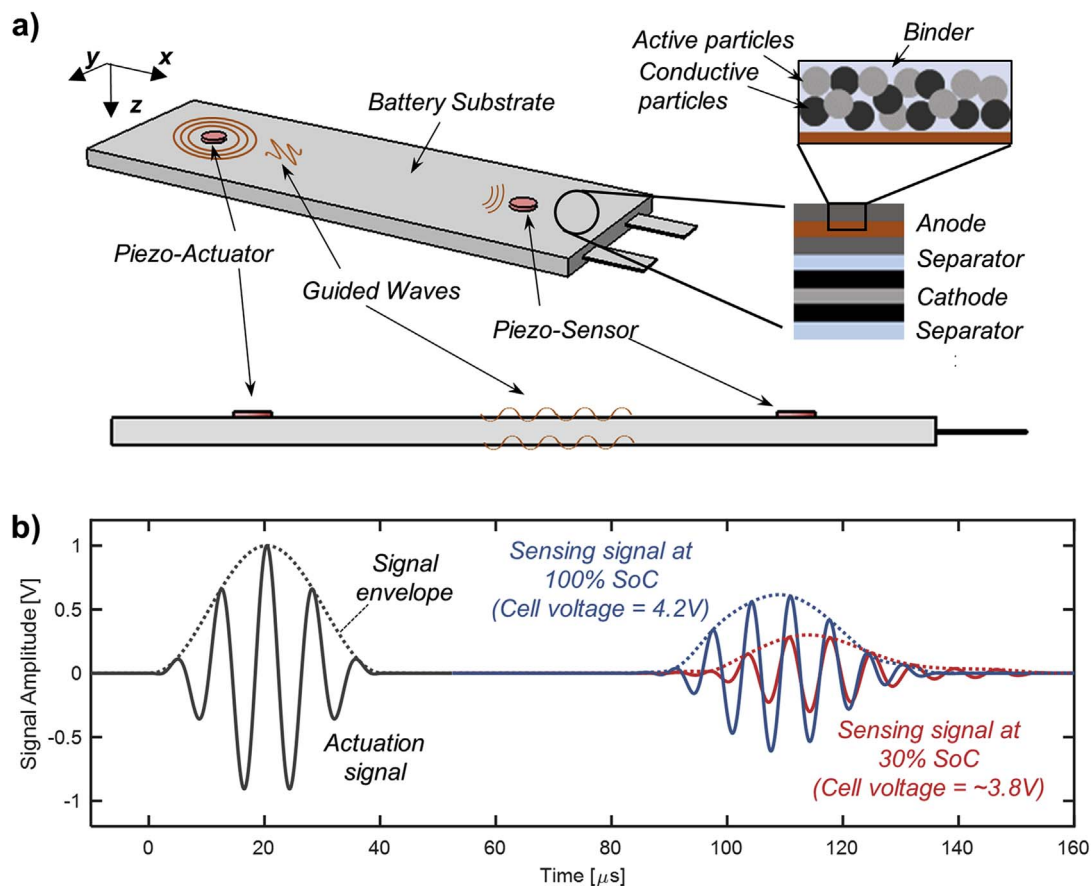


**Fig. 1.** (a) Schematics of the guided wave inspection setup on an indicative Li-ion battery, showing piezoelectric transducers used for pitch-catch guided wave propagation, as well as different internal layers of the battery and constituent materials; (b) representative signals at two SoC, illustrating changes in the receiving signal amplitude (SA) and time of flight (ToF) as a result of changing SoC during charge.

### 3,650 mAh pouch cell

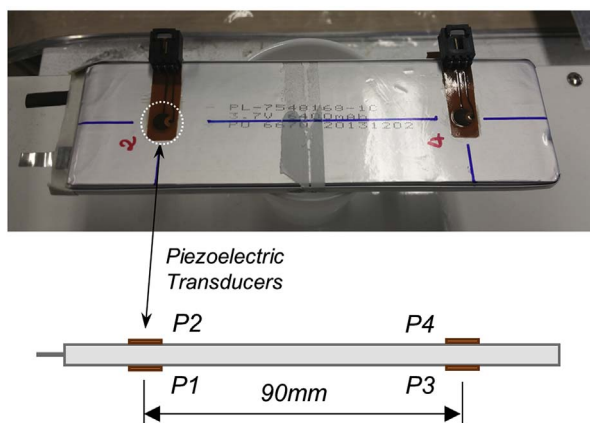


**Fig. 2.** Sensor locations on a 3650 mAh pouch battery. The 6.35 mm-diameter, 0.254 mm-thick piezoelectric disc transducers are labeled P1 through P4.

3650 mAh capacity; 135 × 45 × 5 mm; free-standing and stationary condition).

### 3. Method of approach

To study the proposed problem, both experiments and analysis are carried out. Pitch-catch guided wave propagation experiments are performed on commercial Li-ion pouch batteries using surface-mounted piezoelectric disc transducers. Sensitive ultrasonic features are determined, which correlate

with the distribution of electrode moduli and densities during cycling and aging, and thus with SoC/SoH. The physical relationships between the ultrasonic signature and electrochemical process are thoroughly analyzed. An analytical acoustic model is developed to validate the guided wave response to the changes in electrode moduli and densities during cycling.

The results and physical insights from the experiments and analysis are then used in the preliminary statistical study to evaluate the efficacy of SoC/SoH prediction. A statistical framework is established to explore the feature-rich multi-path nature of guided wave signals for improving prediction accuracy and robustness, as well as for reducing the computational complexity.

### 4. Experimental studies

Guided wave propagation experiments are performed on 3650 mAh off-the-shelf Li-ion pouch batteries (PL-5545135-2C; AA Portable Power Corp.). The 135 × 45 × 5 mm batteries with graphite/nickel-manganese-cobalt oxide (NMC) chemistry are tested as received from the manufacturer, after the standard formation protocol. Guided wave signals are gathered at various SoC and SoH from four surface-mounted piezoelectric disc transducers (6.35 mm-diameter 0.254 mm-thick disc PZT-5A in the SMART Layer format (Acellent Technologies, Inc.)) at the locations shown in Fig. 2. The piezo-transducers are attached on the surface of the batteries with Hysol E-20HP structural epoxy adhesive (Henkel Corp.) using the manufacturer's recommended curing procedure. It is worthwhile noting the significantly smaller footprint of the transducers used in this study, in contrast to the previous work in the literature [32–36].

Guided wave signals are collected in pitch-catch mode [42], whereby one transducer acts as an actuator and the others sense the

incoming waves, resulting in a representative actuator-sensor response, as shown in Fig. 1b. The propagating guided waves interact with the battery medium, allowing the electrochemically-induced changes in electrode moduli and densities to be interrogated during charging, discharging and aging. A total of four propagation paths are under study, i.e., Path 1 from transducer P1 to P3, Path 2 from P1 to P4, Path 3 from P2 to P3, and Path 4 from P2 to P4 (Fig. 2b).

The pitch-catch experiments use standard five-peak Hanning-windowed tone bursts with center frequencies between 100 and 200 kHz. This ensures that we simultaneously diminish wave modes of different velocities, as well as minimize scattering and dispersion in the frequency spectrum [42]. The result is minimal frequency dispersion and modal tuning, allowing repeatable and robust information to be attained with simple signal processing. Additionally, the center frequencies are selected such that a clear wave packet is obtained in the receiving signals. The piezoelectric transducers are actuated and sensed using a 64-channel ultrasonic data acquisition system (ScanGenie II model; Acellent Technologies, Inc.). Ultrasonic measurements are taken every 1 min during electrical charge-discharge cycles. The experiment is carried out with the batteries at a constant temperature in a low-temperature, gravity convection oven.

Two fundamental time-domain parameters are of interest: the signal amplitude (SA), which is the maximum amplitude of the sensing signal's Hilbert envelope [43], and the time of flight (ToF), which is the measure of the time taken by an actuation wave packet to reach a sensor (Fig. 1b). In this work, only the time-domain analysis of the signals is discussed. Nevertheless, addressing the feature-rich nature of guided waves, a thorough feature extraction, spatio-temporal and time-frequency analysis will be presented in a separate future publication.

The ultrasonic data acquisition is synchronized with a high-accuracy battery analyzer (BST-9000 model; Neware Technology Limited), which performs battery charging and discharging, allowing SoC to vary from 0% in the fully discharged state to 100% in the fully charged state. A slow-rate galvanostatic cycling protocol is selected to fully extract anode and cathode phase transition phenomena. In particular, the batteries are cycled at a current rate of C/10, equivalent to 365 mA, at a constant temperature of 30 °C. The rest time between charge and discharge is set to 2 h, without a constant-voltage charge step. ToF and SA are determined from the ultrasonic measurements taken at SoC increments during the charge-discharge process.

To simulate varying SoH, an accelerated aging experiment is performed by aggressively charging and discharging the batteries to evaluate the impact of cell degradation on the guided wave signals. The cells are cycled at an elevated temperature of 45 °C with a constant current rate of 3000 mA (or a current rate of 0.8C, a rate at which the batteries would be fully charged or discharged in 0.8 h) between 3.0 V and 4.2 V. After the constant-current charge, a constant-voltage step is employed with a cutoff value of 182.5 mA (C/20). This ensures that, irrespective of the cycle number, the batteries are brought to full charge (100% SoC). The rest time before the discharge step is 15 min, with no rest period after discharging before the next charge step. A total of 200 charge-discharge cycles are performed. The remaining capacity for each cycle, which is our definition of state of health (SoH), is calculated by evaluating the cycle discharge capacity normalized as a percentage with respect to the value of the first cycle. The slow-rate C/10 is then repeated after the accelerated aging to uncover the electrode degradation behavior and failure modes.

## 5. Analytical acoustic model

An analytical acoustic wave propagation model is used to study the effects of density and modulus variations during battery cycling on the resulting guided wave behavior. The Li-ion pouch cell stack is modelled as a multi-layered material system. The geometry and material properties of the constituent layers are used to formulate the bulk wave propagation problem in each layer. The behavior of the ultrasonic

waves that are guided in the multi-layered system can be determined by considering the interlayer boundary conditions and solving the guided wave equations simultaneously as a system. The solutions to the guided wave problem are in the form of dispersion curves, from which the wave velocity (hence, ToF), attenuation (hence, SA), wave number and other wave characteristics are calculated. The material properties of the individual layers can be varied as a function of SoC, allowing the acoustic response during the galvanostatic cycling to be studied.

The model first starts with formulating the field equations for plane waves in flat isotropic solid layers to relate the stresses and displacements in each of the layers to the corresponding partial waves [44,45]. The governing three-dimensional equations of motions for bulk waves in an infinite medium can be expressed as [44,45]:

$$\rho \frac{\partial^2 \mathbf{u}}{\partial t^2} = (\lambda + \mu) \nabla (\nabla \cdot \mathbf{u}) + \mu \nabla^2 \mathbf{u}$$

where  $\mathbf{u}(u_1, u_2, u_3)$  is the displacement field in the coordinate system  $\mathbf{x}(x_1, x_2, x_3)$  as shown in Fig. 1a,  $\rho$  is the mass density of the material and  $\mu$  and  $\lambda$  are Lamé's stiffness constants, which can also be expressed in terms of Young's modulus ( $E$ ) and Poisson's ratio ( $\nu$ ). If the materials have damping, the wave energy is absorbed as they propagate in the medium [44,45]. A material damping model can be incorporated to describe a constant loss of displacement amplitude per wavelength travelled. The viscoelastic attenuation can be elegantly represented by complex Lamé constants, which are a result of augmenting the real Lamé constants with the material's viscoelastic constants [46–48].

In the case of ultrasonic guided waves (center frequency between 100 and 200 kHz), the wavelengths are significantly smaller than the in-plane dimensions of the pouch cell layers, thus the plane strain assumption holds. The governing equations for each layer can be further reduced to two-dimensional equations only with waves whose particle motion lies entirely in the plane (Lamb type modes) [49,50]. The coupling between layers is achieved by the superposition of the bulk waves while imposing boundary conditions at the layer interfaces. The equation of motions of individual layers are then assembled accordingly into a system of equations, which is solved numerically using the global matrix method [47,51,52]. The solutions to the wave propagation problem correspond to the dispersion curves, from which the wave velocity and attenuation, and hence ToF and SA respectively, can be determined. Once the material properties (stiffness constants, density, and damping properties) and geometry (thickness and stacking sequence) of the individual battery layers have been prescribed, the global matrix method is carried out in the DISPERSE software [48,53], which numerically calculates the dispersion solutions and the wave propagation parameters.

A Li-ion pouch battery is essentially a laminate of active electrode layers, i.e., anode and cathode, stacked in an alternating fashion with each adjacent layer separated by a thin porous polymer separator membrane (Fig. 1a). The anode and cathode themselves are also laminated materials comprising a thin metallic current collector foil (copper and aluminum for anode and cathode respectively) with an active electrode film coating on both sides. The last stage of anisotropy is in the active electrode film, which is a homogeneous mixture of active microparticles (graphite for anode and nickel-manganese-cobalt-oxide for cathode) and electrically conductive particles, adhered together with a polymeric binder.

To initialize the calculation, a functional relationship between SoC and electrodes' moduli and densities needs to be established. The density and modulus values of all the constituent materials are gathered from published resources and are summarized in Table 1 [3,54–56]. The changes in density and modulus of the electrodes are reported in the literature as a function of the lithium content. The mapping between the changes in SoC and lithium content is determined via a separate half-cell experiment. The only parts that are functionally dependent on SoC are the active electrode films (both anode and cathode). The volume-weighted average values of density and modulus of the



**Table 1**  
Material properties used in the DISPERSE simulation.

Components	Thickness [ $\mu\text{m}$ ] <sup>a</sup>	Constituent materials	Volume fraction of constituent materials [%] <sup>b</sup>	Elastic Modulus [GPa]	Density [ $\text{kg m}^{-3}$ ]	Ref.
Anode film	96	Active (graphite)	55	19.2–101.5	2.05–2.26	[54]
		Conductive particles	0	25	1.95	[3]
		Binder	5	2	1.77	[3]
Copper foil	10			100	8	
Cathode film	60	Active (metal oxide)	50.8	108.5–252.1	4.93–5.01	[55,56]
		Conductive particles	8.5	25	1.95	[3]
		Binder	4.7	2	1.77	[3]
Aluminum foil	10			70	2.7	
Separator	25			0.7	0.55	[3]

<sup>a</sup> The layer thicknesses and volume fractions are measured values.

<sup>b</sup> The remaining volume in the active components is filled with organic electrolyte.

electrode films are then calculated using the properties of the constituent particles and their volume fractions. The modulus and density values of all the individual layers, as well as their corresponding layer thickness, are used as input data in the equations of motion, which are solved numerically in the DISPERSE software. The solutions in the form of dispersion curves are then used to calculate the group velocity and ToF as a function of SoC.

The viscoelastic properties of battery materials are not well documented in the traditional electrochemistry literature. The experimental characterization of these properties is a non-trivial exercise but is currently underway. Although the analytical model, in its current form, may be able to predict both ToF and SA, it is assumed that all of the constituent materials are elastic (non-attenuative). The stress waves propagate in the battery system unattenuated; hence, only the ToF as a function of SoC is validated while SA is invariant. Moreover, the analysis involving SA attenuation in an anisotropic, packed particle, laminated material is highly complex. Such analysis is still an active area of research in the community; therefore, the analytical study of signal intensities is worth treating in its entirety in a follow-up publication. Once these data become available, the material properties in the model can be immediately updated to obtain a prediction of SA, in addition to ToF, which is the emphasis of this study.

## 6. Results and discussion

### 6.1. Experimental ultrasonic signature and state of charge

At SoC increments during the C/10 charge-discharge cycle, a five-peak modulated tone burst is propagated from a piezo-actuator. The signal is then received by a piezo-sensor at a different location after a finite amount of time, or ToF. The peak of the signal envelope, or SA, depicts the intensity of the receiving signal. Representative experimental pitch-catch guided wave signals from two different SoC are shown in Fig. 1b, from the P1-P3 transducer pair, with a center frequency of 125 kHz. This illustrates the electrochemically-induced shifts in the signal packets as SoC varies. The same trend is observed across all propagation paths and coupons, showing faster wave speed (smaller ToF) and less signal attenuation (larger SA) as the SoC increases.

Fig. 3 shows the experimental results from extracting and compositing the time-domain signal parameters from guided wave packets measured every 1 min during the C/10 cycle. The pitch-catch ToF and SA are plotted against the cycle elapsed time, demonstrating the shifts in ToF and signal intensity during cycling, and their synchronization with the electrochemical process. As a general trend, ToF shifts towards a smaller value during charge, accompanied by increasing SA. The shift in ToF and SA then reverses during discharge. This cyclic behavior results from an acousto-mechanical phenomenon, wherein the changes in density and modulus distribution of the battery substrate alter the wave propagation characteristics during cycling.

As wave propagation velocity is approximately proportional to the

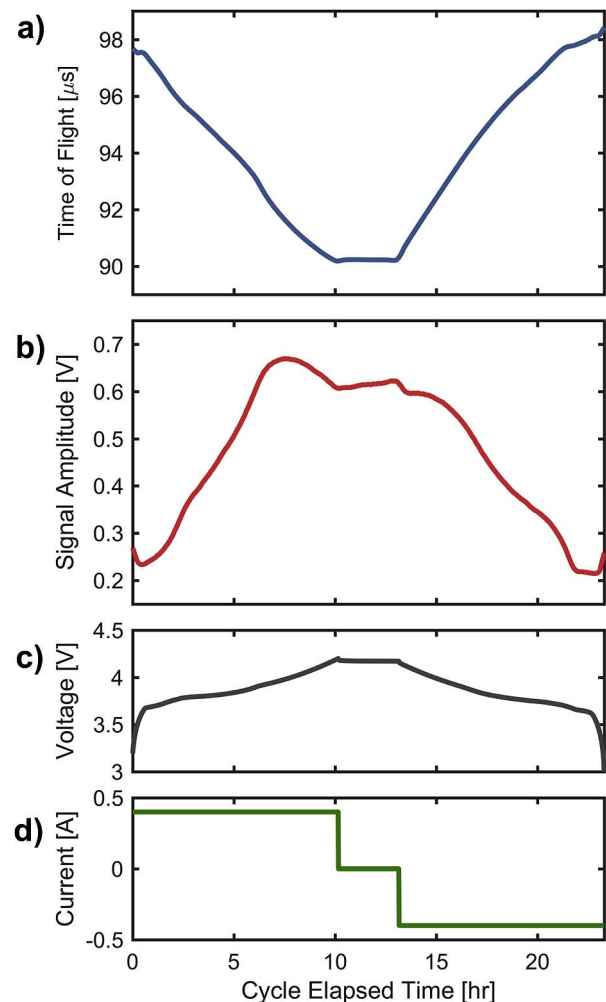


**Fig. 3.** Evolution of a) guided wave ToF and b) SA during a C/10 charge-discharge cycle of a fresh cell. Also shown are c) the corresponding cell voltage and d) current profiles as obtained from the battery cycle. The experimental guided wave data are from the P1-P3 transducer pair, using a tone-burst excitation at 125 kHz.

square root of the modulus-to-density ratio, the decrease in ToF at higher SoC (faster propagation speed) is to be expected from the changes in the modulus and density values shown in Table 1. Despite the counter-intuitive decrease in the cathode modulus, it appears that the aggregate modulus-to-density ratio of the composite still increases as a result of the other three factors: anode modulus and density, and cathode density. This causes the wave to speed up globally (smaller ToF) during charge and slow down (larger ToF) during discharge,

despite the distinct and repeatable local non-linear features observed at various points throughout the cycle (Fig. 3a).

The SA, on the other hand, increases monotonically with SoC for the majority of the cycle with exceptions at near full charge and discharge (Fig. 3b). The signals generally shift towards a larger amplitude for most of the charge process (cell voltage between 3.6 and 4.0 V), and towards a smaller intensity throughout the majority of discharge. However, near 0% and 100% SoC, the SA is seen to decrease with SoC.

Unlike ToF, which is an elastic phenomenon, SA is governed by the substrate's viscoelastic properties. As discussed in Section 5 (Analytical Acoustic Model), the lack of published and validated viscoelastic properties of battery materials makes an analysis of signal attenuation challenging. However, the variation in SA with changing SoC is very notable and is therefore unmistakably a result of varying viscoelastic behavior during cycling. It is hypothesized that as the ions are transferred between the two electrodes, there is an enhancement and relaxation in the lattice strain, which in turn affects the material damping and their attenuation properties. More often than not, a more rigid and compacted material has lower material damping and smaller intrinsic attenuation. The higher aggregate modulus-to-density ratio at higher SoC thereby intuitively leads to reduced attenuation and larger SA.

## 6.2. Differential time of flight and signal amplitude

The local non-linearities observed in the experimental ToF and SA traces deserve special attention. These non-linear signatures are primarily induced by the intercalation staging in the graphitic anode, and potentially in part to the phase transitions of the cathode. Carrying out a similar technique to Differential Voltage Analysis [57–59], the first derivative of ToF and SA with respect to charge capacity ( $d\text{ToF}/dQ$  and  $d\text{SA}/dQ$ , respectively) are calculated and shown in Fig. 4. The non-linear features in ToF and SA are now resolved into highly pronounced peaks and troughs in the differentials. The negative of the  $d\text{ToF}/dQ$  is plotted to accentuate its similarities to  $d\text{SA}/dQ$ .

Comparing the differential ToF and SA with the corresponding differential voltage ( $dV/dQ$ ) in Fig. 4c, the peaks and troughs pertaining to intercalation staging and phase transitioning of the electrodes can be seen to coincide. The two most obvious peaks at approximately 20% and 65% SoC (at 700 and 2200 mAh, respectively) are indicative of the intercalation staging at the anode [60]. Noticeable changes can be observed in the guided wave signal features at the same SoC as a result of the abrupt mechanical activities associated with the staging. The NMC cathode gives the  $dV/dQ$  curve the familiar featureless global convexity due to the rate limitation at extreme SoC [60,61]. This phenomenon results in the globally concave shape of the  $-d\text{ToF}/dQ$  and  $d\text{SA}/dQ$ . This agrees with our prior discussion regarding the softening of the cathode (decreasing modulus) with increasing SoC. That is, at extreme SoC, the rate limitation may cause steep lithium gradients and thus a significant change in the cathode compliance [62]. While we believe this is the case for the cathode, a solid conclusion cannot be drawn and will require further analysis. Nevertheless, this analysis confirms that the evolution in the guided wave signals is indeed reminiscent of the changes in mechanical properties due to the intercalation stages and phase transitions.

## 6.3. Analytical validation of ultrasonic shifts

The effect of battery cycling on the ultrasonic ToF response is computed using an analytical acoustic model described in Section 5 (Analytical Acoustic Model). By varying the electrode moduli and densities as a function of SoC, ToF at a series of time steps during cycling can be determined and compared with the experiment results. The relationship between ToF and SoC is captured with satisfactory accuracy in our analytical acoustic model as demonstrated in Fig. 5. A very good comparison agreement can be seen at higher SoC levels, but overall, the simulation can correctly predict the nominal values of ToF

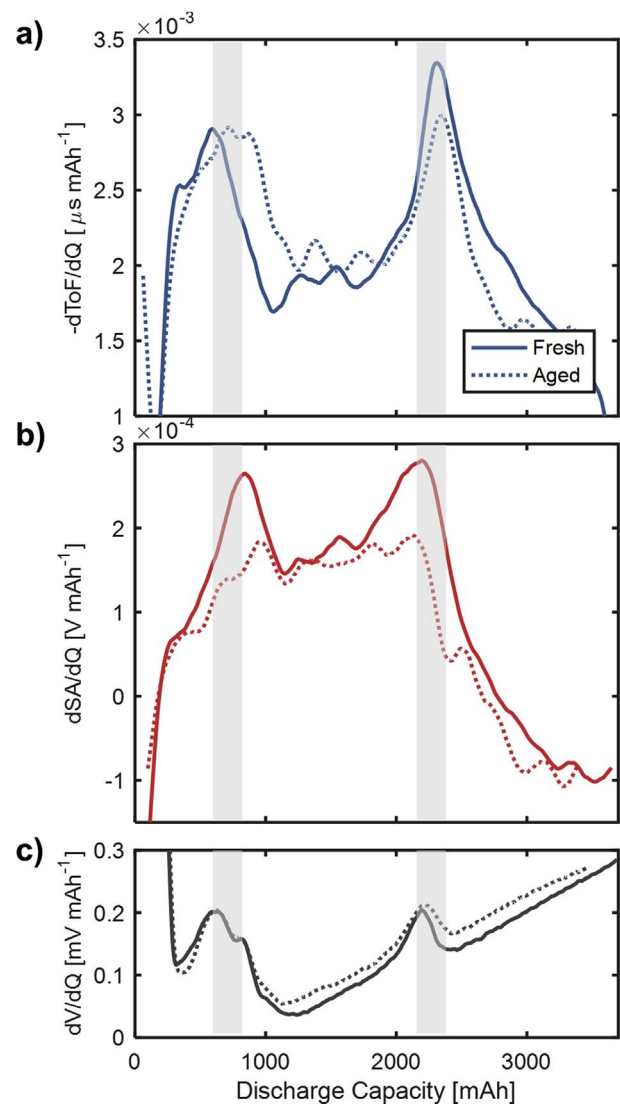


Fig. 4. Differential ToF ( $-d\text{ToF}/dQ$ ) and differential SA ( $d\text{SA}/dQ$ ) of the ToF and SA profiles during the C/10 charge are plotted in panels a) and b), respectively. The corresponding differential voltage ( $dV/dQ$ ) is shown in c). In each panel, two curves are superimposed: the solid line is from a fresh cell, whereas the dotted line is from the same cell after the aging procedure. The guided wave data are from the P1-P3 transducer pair, using a tone-burst excitation at 125 kHz.

as well as the generally decreasing trend with increasing SoC. The absolute change in ToF between the fully charged and discharged states is also predicted reasonably well: approximately 8  $\mu\text{s}$  and 11  $\mu\text{s}$  for the experiment and simulation results, respectively. This finding strongly indicates that the key factors that explain most of the SoC-dependent changes in guided waves are the constituent moduli and densities, and the interplay of their distribution and redistribution.

However, there are local non-linearities observed in the experimental ToF that cannot be accurately captured in the simulation. As mentioned, these non-linearities are primarily induced by the intercalation staging in the graphitic anode, and potentially in part to the concentration-limited phases of the cathode. It is hypothesized that intercalation and phase transitioning cause the changes in the electrode's moduli and densities to be simultaneously enhanced. The local changes in mechanical properties during phase transitions are not well documented in the literature and thus are not included in the current model. We also observe a small discrepancy between the charging and discharging phases in the experimental ToF. Most likely, the modulus and density distribution occur slightly differently during removal and

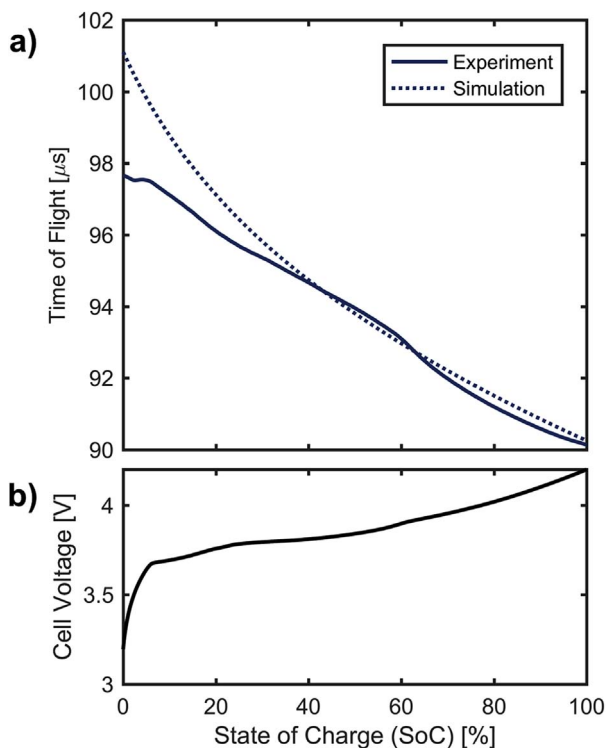


Fig. 5. a) Comparison between ToF from the ultrasonic experiment and the simulated values using the analytical acoustic model during C/10 charge of a representative fresh cell; b) the corresponding cell voltage versus SoC. The guided wave data are from the P1-P3 transducer pair, using a tone-burst excitation at 125 kHz.

insertion of lithium from the graphitic anode into the cathode lattice. As a result, in addition to the assumptions made, the model is still not able to resolve such local non-linearities and hysteretic discrepancies. The charge/discharge rate also affects the rate at which the moduli and densities change, as well as the acousto-elastic effect from the film stress due to intercalation and phase transitions in the active films [63]. Detailed characterization of electrode material properties is currently under investigation. The analytical model, in its current form, can be readily updated as more data on material properties become available.

#### 6.4. Experimental ultrasonic signature and battery aging

Beyond the SoC analysis, the cells are cycled at a faster current rate of 0.8C at an elevated temperature for 200 charge-discharge cycles to simulate the aging process. Fig. 6 shows a composite depiction of the evolution in guided wave behavior throughout the accelerated aging experiment. ToF and SA are calculated from guided wave signals collected every 1 min during the accelerated aging. The signal features are composited and shown as a function of cycle elapsed time. The data are extracted cycle-by-cycle and superimposed to allow convenient observation of the progressive evolution in Fig. 7. Although the ToF and SA change only very slightly from one cycle to the next, it is intriguing that the traces show a repeatable progression and strong correlation with aging. The relationship between guided wave signature and aging indicates that the electrochemical degradation is indeed a mechanical process.

ToF appears to gradually shift towards a smaller nominal value as the cells age, even though the net change within one cycle remains consistent (Figs. 6a and 7a). At the 200th cycle, ToF is nominally smaller by 2  $\mu\text{s}$  at any SoC ( $\sim 2\%$  change). This implies that the aggregate modulus-to-density ratio of the laminate increases in degraded cells. The aging-induced changes in the mechanical properties are indicative of an irreversible transformation in the structure of the electrodes. This can be mainly attributed to the solid electrolyte interface

(SEI) layer formation process, which irreversibly consumes lithium. The SEI interface is known to alter the morphology of the graphite, thus causing the anode modulus and density to change [64,65]. Additionally, the fact that the net change in ToF is almost constant in our experiment suggests that the number of active sites for lithium intercalation remains relatively the same, i.e., minimal loss of active materials. In hindsight, aging of Li-ion batteries is almost always accompanied by irreversible swelling that can be observed visually [66]. For a closed electrochemical cell, the volume expansion results in a reduction in the total mass density, and thereby faster wave speed.

In addition to helping resolve first-order phase transitions, differential voltage analysis is also widely used to effectively pinpoint the degradation root cause and uncover the aging process of Li-ion batteries [57–59]. The same degradation characteristics, as determined from the above ToF analysis, can be inferred from the differential voltage and ToF by comparing the C/10 slow-rate cycles performed before and after the aging experiment (Fig. 4). Pronounced shifts in the peaks of  $d\text{ToF}/dQ$  and  $dV/dQ$  towards higher SoC can be observed, as well as subtle changes in the concavity of the curves. However, the relative distance between the predominant peaks remains the same. This indicates that one main degradation mechanism is the irreversible loss of lithium, most likely due to the SEI layer formation on the graphite anode [67]. The degradation phenomena observed through our differential ToF analysis agree very well with those reported in the literature for high-temperature cycling of graphite/NMC Li-ion batteries, which exhibit lithium loss limiting degradation accompanied by minor cathode capacity loss [60,68–70].

In Figs. 6b and 7b, the aging-induced evolution in SA is more drastic, involving both gradual global shifts and marked changes in local features. As degradation progresses, the SA moves towards a larger nominal value (less attenuation), which is associated with a greater net change in each cycle. While the increase in SA is seen at every SoC, significant signal amplification occurs when the batteries are nearly fully charged. As similarly observed by Hsieh et al. in their work, the end-of-charge signal intensification is attributed to the abrupt changes in the mechanical properties due to localized lithium gradients [34]. The diffusion-limited excess or scarcity of lithium at the interfaces is hypothesized to cause a dramatic compliance change and large lattice strain, which in turn results in decreased signal attenuation.

Moreover, it is important to note that the drop in SA near the end of constant-current charge, which is present in early cycles (marked by A in Fig. 6b), begins to disappear as the batteries degrade (becoming A' and subsequently A'' in Fig. 6b). Irrespective of the cycle number, following the drop or the lack thereof, the SA will start to increase again during the constant-voltage phase. Although less pronounced, the inflection (marked by B in Fig. 6b) at the end of discharge also becomes less noticeable through aging. These provide another indication of the rate-limiting characteristics of charge reception that evolves as a result of aging. The removal of current at the end of constant-current charge relaxes the internal stress and density gradients in the material domains. The relaxation can be seen by the rise in SA following the drop near the end of constant-current charge in early cycles. Over a number of cycles, the residual portion of these internal stresses and density distribution remains, resulting in irreversible changes in the acoustic response. The irreversible mechanical degradation is also observed via the differential SA analysis comparing  $d\text{SA}/dQ$  from a fresh battery with that after aging (Fig. 4b). The two signature anode peaks show significant weakening, which is in agreement with an earlier indication that there are irreversible changes in the anode structure due to SEI layer formation and lithium loss.

#### 6.5. Relationship between state of health and ultrasonic features

Aging causes the charge retention capability of a battery to diminish; i.e., the full discharge capacity, or the remaining capacity, decreases (Fig. 7d). The remaining capacity (normalized full discharge

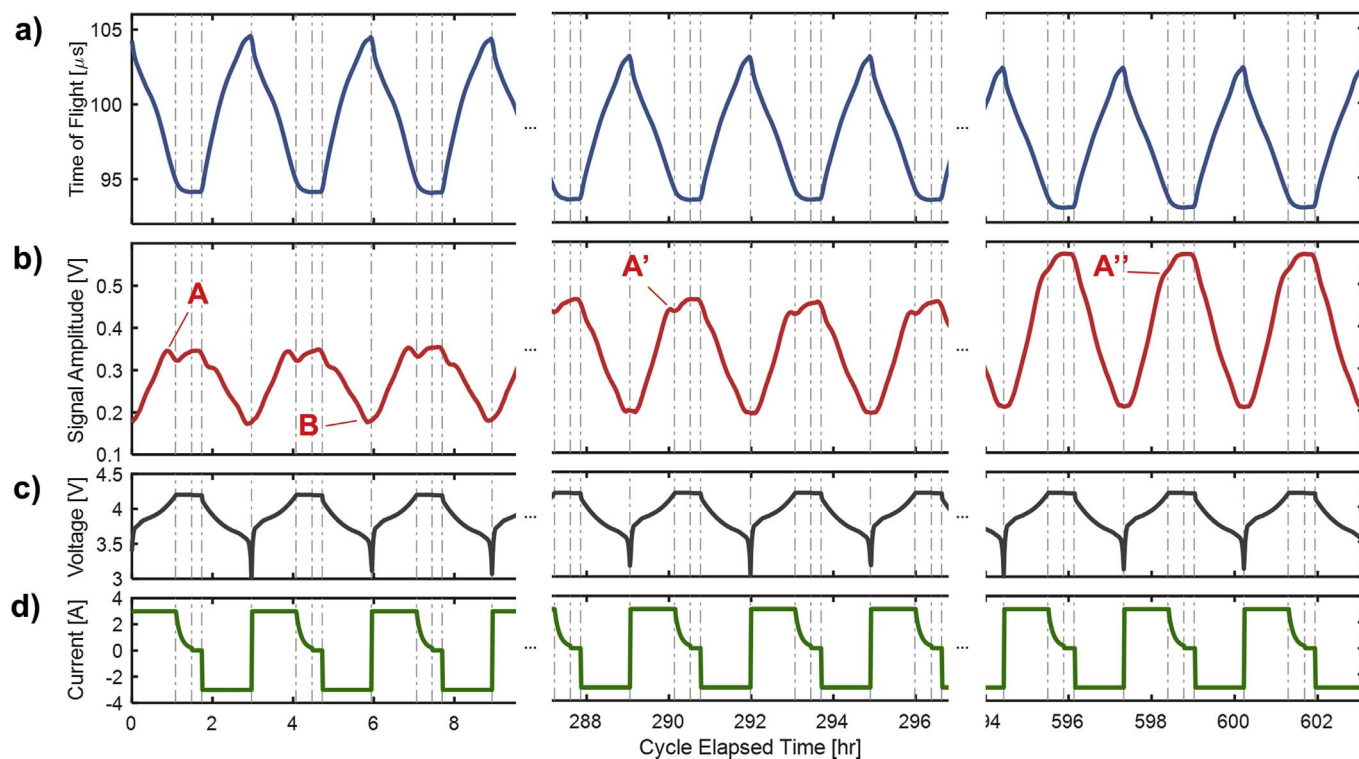


Fig. 6. Composite depiction of the evolution in guided wave behavior throughout the accelerated aging experiment. a) and b) ToF and SA profiles, respectively. c) and d) the corresponding cell voltage and current traces. The vertical gray dashed lines indicate transitions between constant-current charge, constant-voltage charge, rest, and discharge. Features labeled A, A', A'', and B depict the electrode phenomena pertaining to capacity fading, which are discussed in detail in the text.

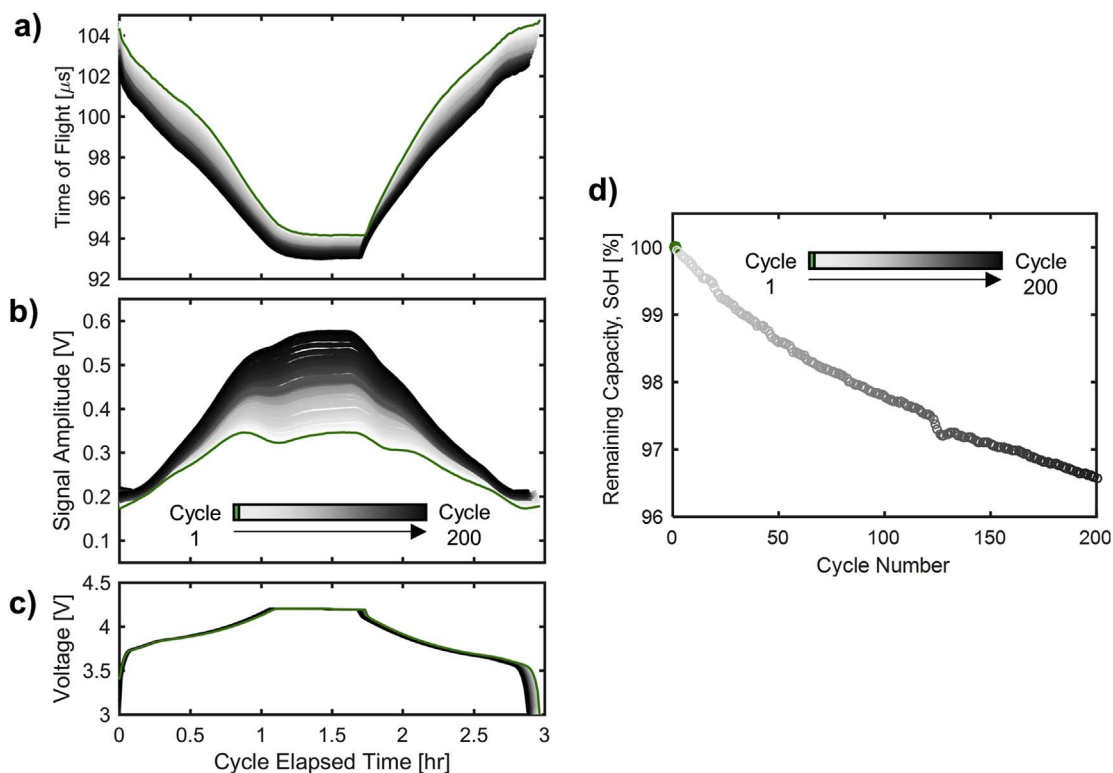
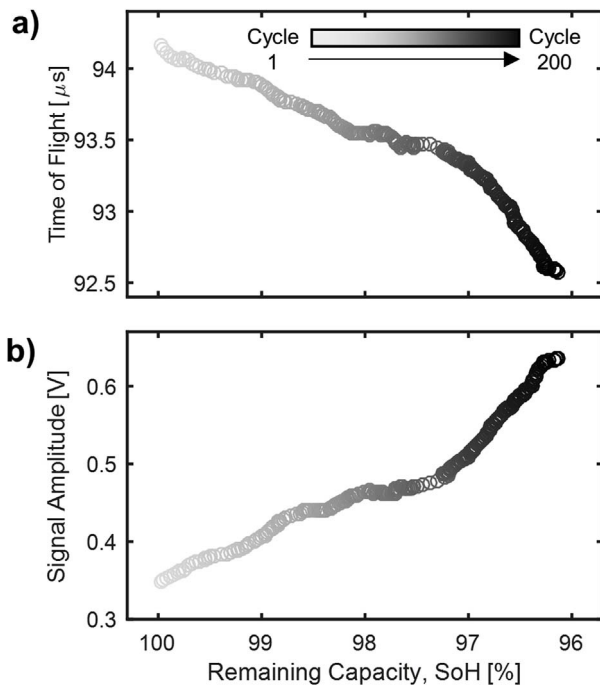


Fig. 7. Cycle-by-cycle evolution of a) ToF and b) SA, as well as c) the corresponding cell voltage. The ToF, SA, and cell voltage data from Fig. 6 are plotted as a function of cycling time for the 0.8C cycles 1 through 200, superimposed cycle-by-cycle. The first cycle (100% SoH) is indicated in green, and progressive shades of gray are used to indicate the increasing number of cycles and the electrochemical aging. d) Capacity retention plot showing remaining capacity (SoH, as a percentage normalized by the first-cycle capacity) with respect to the cycle number throughout the 0.8C (100% DoD) cycling. (For interpretation of the references to colour in this figure legend, the reader is referred to the Web version of this article.)





**Fig. 8.** Guided wave signal features as a function of the remaining capacity (SoH, as a percentage normalized by the first-cycle capacity). a) ToF and b) SA at 100% SoC for cycles 1 through 200. The decrease in the remaining capacity due to cycling, as shown by progressively darker shades of gray, corresponds to the decrease in ToF and increase in SA.

capacity of each cycle with respect to the first cycle capacity) is used as our measure of SoH. In Fig. 7, even during the rest step, where the non-uniformity and rate dependence are relaxed, it is intriguing that strong and repeatable correlations between guided waves and SoH can still be seen. This fundamental finding potentially lays the ground for the development of an accurate in-operation SoH measurement method.

The ToF and SA at the end of the rest period of every cycle are extracted and plotted against SoH in Fig. 8. Regardless of SoH, batteries can be at any SoC by definition. By doing so, we allow the SoH effects on the ultrasonic response to be analyzed while SoC is held constant at 100%. A strong and repeatable correlation can be observed between the guided wave features and SoH. As the degradation takes place, the charge retention capability becomes worse. This electrochemically-induced mechanical aging in turn causes a noticeable reduction in ToF and signal attenuation at the fully-charged relaxed state (approximately 7.5 ns and 1.5 mV per cycle, respectively).

Additionally, the relationships between SoH and the signal features exhibit a subtle but nonetheless important non-linear characteristic. The guided wave signature evolves at an increasingly faster rate as aging transpires. Although not very distinct, the change appears to take place in two stages, with a roll-off approximately at the 100<sup>th</sup> cycle. In agreement with the literature, this confirms that the electrode mechanical degradation manifests at a progressively faster rate throughout the course of aging.

The ability to evaluate battery aging independently from SoC estimation can form the basis for developing an on-board SoH determination technique. In service, when the batteries are fully charged and at rest (e.g. a fully-charged electric vehicle at idle), they can be probed for the guided wave ToF and SA. SoH on target cells can be estimated by comparing the signal parameters with the values from a look-up table pre-collected from an independent set of baseline cells (similar to Fig. 8). In another envisioned situation, this ultrasonic technique is used in conjunction with the traditional voltage measurement on the existing BMS. The latter may be used to initialize the monitoring process by estimating SoC, which, once known, serves as a priori knowledge to

predict and update SoH. With more accurate acousto-mechanical models becoming available through our ongoing research work, a library of training data can be generated which potentially reduces the dependency on laboratory baselines.

Another work in progress is aimed at evaluating the robustness and efficacy of the proposed framework in varying temperature environments. It has been demonstrated nonetheless in the literature that the hardware implementation can operate in a wide range of extreme temperatures [71,72], encompassing the intended operational range of industry-standard Li-ion batteries [5]. However, temperature variations, during fast charging and discharging for instance, can still affect the material properties of the substrate, adhesive, and transducers. As with all ultrasonic NDE/SHM techniques, the resulting changes in the acoustic wave propagation may lead to a disparity in waveforms if not properly compensated. The NDE/SHM research community has actively addressed the challenges of varying temperature and proposed numerous strategies, from data-driven techniques [73–75] to analytical models [76,77], that can effectively compensate for temperature effects.

The authors also have recently developed and validated a physics-based temperature compensation model for ultrasonic guided wave SHM [78,79]. Analytical studies of wave propagation provide useful physical insight that can be coupled with data-driven strategies to efficiently and accurately compensate for the temperature influence. The model utilizes the Matching Pursuit time-frequency representation to project waveforms into representative atoms [80]. With physical insight of the underlying system, a very limited set of baseline data can be used to create a functional relationship between the projection coefficients of the atoms and the material properties under varying temperatures. Temperature-compensated signals can be accurately reconstructed from a new set of projection coefficients estimated at a target temperature [78,79]. It is anticipated that a similar strategy can be immediately applied to compensate for temperature effects for battery monitoring.

## 7. SoC/SoH prediction

### 7.1. Statistical method

This part of the work aims at exploiting the *multi-path, feature-rich nature of guided wave signals* to obtain accurate real-time SoC/SoH estimations. Therefore, we conduct a fundamental statistical analysis and validate the feasibility of: (i) improving the prediction accuracy by simultaneously using two ultrasonic features (ToF and SA); (ii) further reducing prediction error by using information from multiple paths; and (iii) reducing the prediction model order without losing accuracy by maintaining data richness.

A basic statistical analysis is performed by creating prediction models based on a Generalized Additive Model (GAM) [81]. GAMs are a semi-parametric regression technique that allows dependent variables to be described by smooth non-linear functions of covariates. GAMs with a Gaussian error distribution and identical link function are fitted to the collected data set to estimate SoC and SoH (dependent variables). Thin-plate regression splines are employed as smoothed non-linear fits of covariates using maximum penalized likelihood to prevent over-fitting [82–84]. For each GAM, different sets of covariates are considered:

- Model 1: the only covariate is the ToF from Path 1 (P1 to P3) at 125 kHz (1 predictor).
- Model 2: the only covariate is the SA from Path 1 at 125 kHz (1 predictor).
- Model 3: ToF and SA from Path 1 at 125 kHz are the covariates (2 predictors).
- Model 4: ToF and SA from Paths 1 through 4 at 125 kHz are the covariates (8 predictors).
- Model 5: the same covariates as Model 4, but the maximum degrees

of freedom (df) of each smoothed fit is limited to 2 [84] (8 predictors, limited df).

The above five model structures are then statistically compared to validate the use of multiple features and paths. The deviance explained, adjusted  $R^2$ , and Akaike Information Criterion (AIC) [85] are calculated and compared for each of the models. The fitted models are then applied to the validation dataset to compare the predicted and measured SoC and SoH. From which, the generalized cross-validation score (GCV), as well as the 10-fold cross validation (CV) error, can be evaluated to reinforce the model comparison in addition to the use of classic statistical criteria. The GAM analysis uses the 'mgcv' package (version 1.8–18) in R.

For SoC prediction ( $SoC \sim fn(ToF, SA)$ ), the model is trained and applied to aggregate data from healthy cells prior to the accelerated aging. That is, SoH is held constant during the estimation of SoC. The SoH prediction ( $SoH \sim fn(ToF, SA)$ ) is performed using the ToF and SA data at the fully-charged state of each cycle (SoC independent). SoH can be predicted at intermediate SoC and vice versa via co-estimation or compensation, as demonstrated in the literature [5,86,87]; however, such treatment will not be elaborated on as part of this work.

## 7.2. Statistical results

To elaborate on the first aim (improving the prediction accuracy by simultaneously using two ultrasonic features: ToF and SA), we evaluate the statistical results from Models 1 through 3. The GAMs and their statistical values for a representative pouch cell are presented in Tables 2 and 3 for SoC and SoH prediction, respectively. Using both ToF and SA as predictors, Model 3 shows better prediction accuracy (lower AIC, GCV score, and 10-fold CV error) than Models 1 and 2. This is true for all other signal paths, which are not shown here for the sake of brevity. Therefore, this confirms the feasibility of exploiting the feature-rich nature of guided wave data for SoC/SoH prediction accuracy improvement. An average prediction error from Model 3 (as evaluated through the GCV score and 10-fold CV error) is as low as < 0.5% and < 0.01% for SoC and SoH predictions, respectively.

A comparison between Models 1 and 2 indicates that ToF appears to be a better predictor of SoC/SoH than SA. This is to be expected owing to the higher noise level and the abrupt changes in the curvature in the SA versus SoC plot (Fig. 3b). Yet, they are both statistically significant in improving the prediction accuracy in the multi-variate Model 3 (p-value < 0.001). Feature extraction and selection thus become crucial, and care should be taken when constructing a prediction model using multiple signal features. This is particularly important when this

technique is extended beyond time domain features, involving complex predictors such as extracted features from time-frequency representation.

Model 3 is compared to Model 4 to investigate the added benefits of using an ensemble of data from multiple paths. With ToF and SA data from four distinct propagation paths, Model 4 (8 predictors: ToF and SA from all four paths) exhibits significantly better prediction accuracy. All but one predictor in Model 4 are statistically significant (p-value < 0.001) and thus contribute to the SoC prediction accuracy improvement. Using Model 4, the prediction accuracy (GCV score and 10-fold CV error) drops startlingly to well below 0.1% and 0.005% for SoC and SoH predictions, respectively.

Model 5 keeps the same predictors as Model 4, but the maximum df of each functional relationship is limited to 2. The prediction of accuracy of Model 5 is similar to that of Model 3, which uses two predictors without any limitation on the df (average error of ~ 0.5% for SoC prediction, and ~ 0.006% for SoH). However, the structure of Model 5 involves much fewer df than Model 3 (2-fold decrease in model complexity). This presents an opportunity for reducing the prediction model order by exploiting the multi-dimensionality of guided wave data, allowing good prediction accuracy to be achieved with low computational cost.

The contribution of different error sources towards SoC/SoH prediction is presented in Table 4. The errors in ToF and SA ( $\Delta ToF$  and  $\Delta SA$ , respectively) are determined for each error source, and these errors are used to perturb the predictors in Model 3 to estimate the expanded prediction uncertainty. In the current setting, the prediction models are trained on data from independent baseline cycles on the same given cells. Therefore, the error is contributed to by two main external sources: measurement error and temperature effect. The combined effect explains most of the prediction uncertainty. The measurement error, which encompasses the noise and error of the front-end electronics and sensors, accounts for more than 60% of the prediction error. The temperature variations ( $\pm 0.2^\circ\text{C}$ ) during experiments create a linear response in  $\Delta ToF$  and  $\Delta SA$ , which explain the rest of the prediction error. The expanded uncertainty is also found to be in the same order of magnitude as the prediction errors calculated from Model 3 using actual experimental data. Albeit a crucial aspect, the uncertainty propagation in different model structures is not a linear exercise and is far more challenging to be addressed with existing results. To enable the use of separate baseline cells for training, the error sources intrinsic to individual cells (cell-to-cell variation on battery material properties, sensor locations, sensor/adhesive properties, etc.) need to be analyzed in detail [88]. The wider, realistic temperature range also signifies the foregoing temperature compensation strategy

**Table 2**  
Statistical results of the different SoC prediction models.

Parameters	Model 1		Model 2		Model 3		Model 4		Model 5	
Adjusted $R^2$	0.999		0.991		1		1		1	
Deviance explained (%)	99.9		99.1		100		100		100	
GCV score	0.947		7.87		0.265		0.057		0.331	
AIC	1647		2899		895		–19		1026	
global df	10.9		10.6		19.2		43.6		9.57	
10-fold CV error	1.01		7.87		0.45		0.09		0.44	
	df	p-value	df	p-value	df	p-value	df	p-value	df	p-value
Covariates										
Path 1 ToF	8.92	< 0.001	–	–	9	< 0.001	6.78	< 0.001	1.84	< 0.001
Path 1 SA	–	–	8.56	< 0.001	8.16	< 0.001	0.13	0.323	0.38	< 0.001
Path 2 ToF	–	–	–	–	–	–	7.28	< 0.001	1	< 0.001
Path 2 SA	–	–	–	–	–	–	6.96	< 0.001	1.46	< 0.001
Path 3 ToF	–	–	–	–	–	–	6.51	< 0.001	0.54	< 0.01
Path 3 SA	–	–	–	–	–	–	7.45	< 0.001	1	< 0.001
Path 4 ToF	–	–	–	–	–	–	3.12	< 0.001	0.99	< 0.001
Path 4 SA	–	–	–	–	–	–	3.4	< 0.001	0.37	< 0.001

Approximate significance levels (p-value) and degrees of freedom (df) are displayed for each of the covariates.

**Table 3**  
Statistical results of the different SoH prediction models.

Parameters	Model 1		Model 2		Model 3		Model 4		Model 5	
Adjusted R <sup>2</sup>	0.994		0.961		0.995		0.997		0.995	
Deviance explained (%)	99.4		96.2		99.5		99.8		99.5	
GCV score	0.0069		0.0448		0.0057		0.0034		0.0057	
AIC	−522		−64		−569		−570		−703	
global df	10.4		9.2		16.2		35.4		9.1	
10-fold CV error	0.007		0.0436		0.0057		0.0038		0.0059	
	df	p-value	df	p-value	df	p-value	df	p-value	df	p-value
Covariates										
Path 1 ToF	8.36	< 0.001	–	–	7.78	< 0.001	6.46	< 0.001	0.69	< 0.001
Path 1 SA	–	–	7.2	< 0.001	6.43	< 0.001	6.20	< 0.001	1.08	< 0.001
Path 2 ToF	–	–	–	–	–	–	4.30	< 0.01	0.34	< 0.001
Path 2 SA	–	–	–	–	–	–	1.49	1.00	1.81	< 0.001
Path 3 ToF	–	–	–	–	–	–	6.68	< 0.001	0	< 0.001
Path 3 SA	–	–	–	–	–	–	4.82	< 0.001	0.86	< 0.001
Path 4 ToF	–	–	–	–	–	–	3.43	< 0.001	0.38	< 0.001
Path 4 SA	–	–	–	–	–	–	0	0.63	1.99	< 0.001

Approximate significance levels (p-value) and degrees of freedom (df) are displayed for each of the covariates.

**Table 4**  
Error flowchart showing the expanded uncertainty in the SoC and SoH prediction owing to contributions from different error sources.

Error Sources	Expanded Uncertainty (RMSE %) in	
	SoC	SoH
Measurement error	0.61	0.0049
$\Delta\text{ToF} \sim N(0, 4.8 \times 10^{-4}) \mu\text{s}$		
$\Delta\text{SA} \sim N(0, 6.40 \times 10^{-5}) \text{V}$		
Temperature effect	0.29	0.0016
$\Delta\text{ToF} = 0.122\Delta\text{T} \mu\text{s}$		
$\Delta\text{SA} = 0.012\Delta\text{T} \text{V}$		
where $\Delta\text{T} \sim U(-0.2, 0.2) ^\circ\text{C}$		
Combined effect	0.69	0.0051

RMSE denotes ‘root-mean-square error’.

$N(\cdot, \cdot)$  denotes normal distribution with the indicated mean and variance.

$U(\cdot, \cdot)$  denotes uniform distribution with the indicated minimum and maximum.

(Section 6.5).

All in all, we have presented a first-pass statistical analysis of guided wave data with an attempt to explore the multi-feature, multi-path nature of guided wave signals for battery SoC/SoH prediction. It is important to note that this analysis is model-agnostic and is merely used to emphasize the benefits of this method over the scalar voltage measurement in a traditional BMS. Nevertheless, it is shown that guided waves can be applied in conjunction with voltage-based prediction to reduce the dependence on data history and further improve the state estimation robustness and accuracy. Together with a well-established ‘metric’ for SoC/SoH, this technique has shown potential as a foundation for creating a unified predictive model for real-time battery state estimation.

## 8. Conclusions

This work established a preliminary evaluation of estimating battery SoC/SoH with ultrasonic guided waves. Experimental pitch-catch guided wave propagation was conducted on commercial Li-ion pouch batteries retrofitted with low-profile surface-mounted piezo transducers. The results obtained suggested that this technique can potentially form the basis for developing an effective method for SoC/SoH estimation. Similar techniques may be applied not only to Li-ion cells, but also to batteries of various chemistries, scales, and form factors. Most importantly, we have also demonstrated the field applicability using miniscule transducers and simple signal processing, which offer a

significant improvement over the state-of-the-art ultrasonic techniques for battery interrogation. In sum, our study has shown that:

- The changes in guided wave signal features provide an indication of the physical processes during a charge-discharge cycle, which can be directly correlated with battery SoC. Guided wave ToF and SA reveal the progression of the electrode modulus and density distribution as a result of the intertwined electrochemical-mechanical coupling. Besides SoC, the guided wave measurements are also able to uncover the underlying electrochemical signature, e.g., intercalation staging and phase transitioning.
- The global stiffening and expansion of the electrode laminate are found to be the main contributing factors to the changes in wave speed. By varying the electrode moduli and densities in our acoustic model, the nominal magnitude and range of experimental ToF during cycling are accurately validated. With more precise mechanical property measurements, it is believed that the model will be able to resolve the local non-linearities and rate dependence. Yet, our current model is able to describe the majority of the acoustic activities and significantly strengthen the understanding of the proposed technique.
- ToF and SA are also found to vary as a function of cycle number, which infers the mechanical nature of battery aging. Complimentary to traditional voltage-based methods, given a known SoC, battery SoH can be directly estimated using correlations from guided wave measurements. Beyond SoH prediction, guided wave signature is also indicative of the underlying degradation mechanisms.
- A preliminary statistical analysis has shown that SoC/SoH can be accurately predicted using guided wave data on-demand, without relying on data history. Moreover, we have shown the potential of exploiting the feature-rich, multi-path nature of guided wave signals to enhance prediction accuracy and to reduce prediction model order.

Future work involves spatio-temporal and time-frequency analysis of guided waves to improve the robustness and accuracy of state prediction. We will also explore the use of state-of-the-art guided wave inspection techniques, such as modal tuning, operational effect compensation, and so forth. More detailed investigation is underway for incorporating fully characterized material properties into our acoustic model. The refined model will help generate training sets of electrochemical cells with hypothetical cycling and aging mechanisms, which will serve as a baseline and allow thorough validation of the statistical prediction models. As with guided-wave-based SHM, the concept can also be extended and applied to structurally-integrated energy storage,

a concept newly introduced in the literature [40,89,90], for simultaneous structural and battery state monitoring.

## Acknowledgements

The work is supported by the Advanced Research Projects Agency - Energy [grant number DE-AR0000393] and the Stanford Precourt Institute of Energy. The authors highly appreciate support from Dr. Keith Kepler, Dr. Hongjian Liu, and Dr. Michael Slater at Farasis Energy, Inc., as well as Mr. Raphael Nardari at Zenith Aerospace for valuable feedback and suggestions. We would also like to thank Accellent Technologies Inc. for providing necessary hardware support for the experiments conducted in this research.

## References

- J.B. Goodenough, K.-S. Park, The Li-Ion rechargeable battery: a perspective, *J. Am. Chem. Soc.* 135 (4) (2013) 1167–1176.
- P. Liu, R. Ross, A. Newman, Long-range, low-cost electric vehicles enabled by robust energy storage, *MRS Energy & Sustainability* (2015) 2.
- D. Linden, *Handbook of Batteries*, In Fuel and Energy Abstracts, (1995).
- V. Etacheri, et al., Challenges in the development of advanced Li-ion batteries: a review, *Energy Environ. Sci.* 4 (9) (2011) 3243–3262.
- L. Lu, et al., A review on the key issues for lithium-ion battery management in electric vehicles, *J. Power Sources* 226 (2013) 272–288.
- X. Hu, et al., Battery health prognosis for electric vehicles using sample entropy and sparse Bayesian predictive modeling, *IEEE Trans. Ind. Electron.* 63 (4) (2016) 2645–2656.
- X. Hu, et al., Technological developments in batteries: a survey of principal roles, types, and management needs, *IEEE Power Energy Mag.* 15 (5) (2017) 20–31.
- W. Waag, C. Fleischer, D.U. Sauer, Critical review of the methods for monitoring of lithium-ion batteries in electric and hybrid vehicles, *J. Power Sources* 258 (2014) 321–339.
- J. Zhang, J. Lee, A review on prognostics and health monitoring of Li-ion battery, *J. Power Sources* 196 (15) (2011) 6007–6014.
- S.M. Rezvanianani, et al., Review and recent advances in battery health monitoring and prognostics technologies for electric vehicle (EV) safety and mobility, *J. Power Sources* 256 (2014) 110–124.
- X. Hu, et al., Enhanced sample entropy-based health management of Li-ion battery for electrified vehicles, *Energy* 64 (2014) 953–960.
- Z. Lu, J.R. Dahn, Understanding the anomalous capacity of Li/Li [Ni x Li (1/3 – 2x/3) Mn (2/3 – x/3)] O 2 cells using in situ X-ray diffraction and electrochemical studies, *J. Electrochem. Soc.* 149 (7) (2002) A815–A822.
- K.W. Nam, et al., Combining in situ synchrotron x-ray diffraction and absorption techniques with transmission electron microscopy to study the origin of thermal instability in overcharged cathode materials for lithium-ion batteries, *Adv. Funct. Mater.* 23 (8) (2013) 1047–1063.
- X.-J. Wang, et al., A new in situ synchrotron X-ray diffraction technique to study the chemical delithiation of LiFePO 4, *Chem. Commun.* 47 (25) (2011) 7170–7172.
- N. Sharma, et al., Structural changes in a commercial lithium-ion battery during electrochemical cycling: an in situ neutron diffraction study, *J. Power Sources* 195 (24) (2010) 8258–8266.
- X.-L. Wang, et al., Visualizing the chemistry and structure dynamics in lithium-ion batteries by in-situ neutron diffraction, *Sci. Rep.* 2 (2012) 747.
- U. Tröltzsch, O. Kanoun, H.-R. Tränkle, Characterizing aging effects of lithium ion batteries by impedance spectroscopy, *Electrochim. Acta* 51 (8) (2006) 1664–1672.
- W. Waag, S. Käbitz, D.U. Sauer, Experimental investigation of the lithium-ion battery impedance characteristic at various conditions and aging states and its influence on the application, *Appl. Energy* 102 (2013) 885–897.
- K.S. Ng, et al., Enhanced coulomb counting method for estimating state-of-charge and state-of-health of lithium-ion batteries, *Applied energy* 86 (9) (2009) 1506–1511.
- S.J. Moura, N.A. Chaturvedi, M. Krstić, Adaptive partial differential equation observer for battery state-of-charge/state-of-health estimation via an electrochemical model, *J. Dyn. Syst. Meas. Contr.* 136 (1) (2014) 011015.
- X. Hu, S. Li, H. Peng, A comparative study of equivalent circuit models for Li-ion batteries, *J. Power Sources* 198 (2012) 359–367.
- G.L. Plett, Extended Kalman filtering for battery management systems of LiPB-based HEV battery packs: Part 3. State and parameter estimation, *J. Power Sources* 134 (2) (2004) 277–292.
- V. Klass, M. Behm, G. Lindbergh, A support vector machine-based state-of-health estimation method for lithium-ion batteries under electric vehicle operation, *J. Power Sources* 270 (2014) 262–272.
- C. Sbarufatti, et al., Adaptive prognosis of lithium-ion batteries based on the combination of particle filters and radial basis function neural networks, *J. Power Sources* 344 (2017) 128–140.
- M. Dubarry, et al., Incremental capacity analysis and close-to-equilibrium OCV measurements to quantify capacity fade in commercial rechargeable lithium batteries, *Electrochem. Solid State Lett.* 9 (10) (2006) A454–A457.
- C. Weng, et al., On-board state of health monitoring of lithium-ion batteries using incremental capacity analysis with support vector regression, *J. Power Sources* 235 (2013) 36–44.
- G. Liu, et al., Online estimation of lithium-ion battery remaining discharge capacity through differential voltage analysis, *J. Power Sources* 274 (2015) 971–989.
- L. Wang, et al., On-board state of health estimation of LiFePO 4 battery pack through differential voltage analysis, *Appl. Energy* 168 (2016) 465–472.
- T. Kundu, *Ultrasonic Nondestructive Evaluation: Engineering and Biological Material Characterization*, CRC press, 2003.
- V. Giurgiutiu, *Structural Health Monitoring: with Piezoelectric Wafer Active Sensors*, Academic Press, 2007.
- A. Raghavan, C.E. Cesnik, Review of guided-wave structural health monitoring, *Shock Vib. Digest* 39 (2) (2007) 91–116.
- Sood, B., M. Osterman, and M. Pecht. Health monitoring of lithium-ion batteries. in *Product Compliance Engineering (ISPC)*, 2013 IEEE Symposium on. 2013. IEEE.
- S. Bhadra, *Methods for Characterization of Batteries Using Acoustic Interrogation*, Princeton University, 2015.
- A. Hsieh, et al., Electrochemical-acoustic time of flight: in operando correlation of physical dynamics with battery charge and health, *Energy Environ. Sci.* 8 (5) (2015) 1569–1577.
- G. Davies, et al., State of charge and state of health estimation using electrochemical acoustic time of flight analysis, *J. Electrochem. Soc.* 164 (12) (2017) A2746–A2755.
- L. Gold, et al., Probing lithium-ion batteries' state-of-charge using ultrasonic transmission—Concept and laboratory testing, *J. Power Sources* 343 (2017) 536–544.
- J.L. Rose, *Ultrasonic guided waves in structural health monitoring*, Key Engineering Materials, Trans Tech Publ, 2004.
- A. Güemes, SHM technologies and applications in aircraft structures, *Proceedings of the 5th International Symposium on NDT in Aerospace*, Singapore, 2013, pp. 13–15.
- Z. Su, L. Ye, Y. Lu, Guided Lamb waves for identification of damage in composite structures: a review, *J. Sound Vib.* 295 (3) (2006) 753–780.
- P. Ladpli, et al., Design of multifunctional structural batteries with health monitoring capabilities, *European Workshop on Structural Health Monitoring 2016*, 2016 (Bilbao, Spain).
- P.K. Ladpli, Nardari Fotis, Chang Raphael, Fu-Kuo, Battery charge and health state monitoring via ultrasonic guided-wave-based methods using built-in piezoelectric transducers, *SPIE Smart Structures/NDE 2017*, 2017 (Portland, OR).
- J.-B. Ihn, F.-K. Chang, Pitch-catch active sensing methods in structural health monitoring for aircraft structures, *Struct. Health Monit.* 7 (1) (2008) 5–19.
- M. Feldman, Hilbert transform in vibration analysis, *Mechanical Systems and Signal Processing* 25 (3) (2011) 735–802.
- H. Kolsky, *Stress Waves in Solids* vol 1098, Courier Corporation, 1963.
- J. Achenbach, *Wave Propagation in Elastic Solids* vol 16, Elsevier, 2012.
- T.H. Watson, A real frequency, complex wave-number analysis of leaking modes, *Bull. Seismol. Soc. Am.* 62 (1) (1972) 369–384.
- M.J. Lowe, Matrix techniques for modeling ultrasonic waves in multilayered media, *IEEE Trans. Ultrason. Ferroelectrics Freq. Contr.* 42 (4) (1995) 525–542.
- B. Pavlakovic, M. Lowe, *Disperse User's Manual Version 2.0*, 11, Imperial College, Univ of London, 2001.
- H. Lamb, On waves in an elastic plate, *Proceedings of the Royal Society of London a: Mathematical, Physical and Engineering Sciences*, 1917 (The Royal Society).
- A.E.H. Love, *Some Problems of Geodynamics*, Cambridge University Press, 2015.
- L. Knopoff, A matrix method for elastic wave problems, *Bull. Seismol. Soc. Am.* 54 (1) (1964) 431–438.
- M.J. Randall, Fast programs for layered half-space problems, *Bull. Seismol. Soc. Am.* 57 (6) (1967) 1299–1315.
- B. Pavlakovic, et al., *Disperse: A General Purpose Program for Creating Dispersion Curves*, in *Review of Progress in Quantitative Nondestructive Evaluation*, Springer, 1997, pp. 185–192.
- Y. Qi, et al., Threefold increase in the Young's modulus of graphite negative electrode during lithium intercalation, *J. Electrochem. Soc.* 157 (5) (2010) A558–A566.
- B. Rieger, et al., A new method to model the thickness change of a commercial pouch cell during discharge, *J. Electrochem. Soc.* 163 (8) (2016) A1566–A1575.
- L. Wu, J. Zhang, Ab initio study of anisotropic mechanical properties of LiCoO2 during lithium intercalation and deintercalation process, *J. Appl. Phys.* 118 (22) (2015) 225101.
- I. Bloom, et al., Differential voltage analyses of high-power, lithium-ion cells: 1. Technique and application, *Journal of Power Sources* 139 (1) (2005) 295–303.
- H.M. Dahn, et al., User-friendly differential voltage analysis freeware for the analysis of degradation mechanisms in Li-ion batteries, *J. Electrochem. Soc.* 159 (9) (2012) A1405–A1409.
- Y. Zhang, C.-Y. Wang, X. Tang, Cycling degradation of an automotive LiFePO 4 lithium-ion battery, *J. Power Sources* 196 (3) (2011) 1513–1520.
- I. Bloom, et al., Differential voltage analyses of high-power lithium-ion cells. 4. Cells containing NMC, *J. Power Sources* 195 (3) (2010) 877–882.
- R.D. Deshpande, et al., The limited effect of VC in graphite/NMC cells, *J. Electrochem. Soc.* 162 (3) (2015) A330–A338.
- X. Zhang, A.M. Sastry, W. Shyy, Intercalation-induced stress and heat generation within single lithium-ion battery cathode particles, *J. Electrochem. Soc.* 155 (7) (2008) A542–A552.
- N. Gandhi, J.E. Michaels, S.J. Lee, Acoustoelastic Lamb wave propagation in biaxially stressed plates, *J. Acoust. Soc. Am.* 132 (3) (2012) 1284–1293.
- P.B. Balbuena, Y. Wang, *Lithium-ion Batteries: Solid-electrolyte Interphase*, World Scientific, 2004.
- M. Broussely, et al., Main aging mechanisms in Li ion batteries, *J. Power Sources* 146 (1) (2005) 90–96.
- J. Cannarella, C.B. Arnold, Stress evolution and capacity fade in constrained



- lithium-ion pouch cells, *J. Power Sources* 245 (2014) 745–751.
- [67] R. Deshpande, et al., Battery cycle life prediction with coupled chemical degradation and fatigue mechanics, *J. Electrochem. Soc.* 159 (10) (2012) A1730–A1738.
- [68] K. Jalkanen, et al., Cycle aging of commercial NMC/graphite pouch cells at different temperatures, *Appl. Energy* 154 (2015) 160–172.
- [69] J. Wang, et al., Degradation of lithium ion batteries employing graphite negatives and nickel–cobalt–manganese oxide + spinel manganese oxide positives: Part 1, aging mechanisms and life estimation, *J. Power Sources* 269 (2014) 937–948.
- [70] J. Cannarella, C.B. Arnold, State of health and charge measurements in lithium-ion batteries using mechanical stress, *J. Power Sources* 269 (2014) 7–14.
- [71] X.P. Qing, et al., The performance of a piezoelectric-sensor-based SHM system under a combined cryogenic temperature and vibration environment, *Smart Mater. Struct.* 17 (5) (2008) 055010.
- [72] V. Giurgiutiu, B. Xu, W. Liu, Development and testing of high-temperature piezoelectric wafer active sensors for extreme environments, *Struct. Health Monit.* 9 (6) (2010) 513–525.
- [73] T. Clarke, F. Simonetti, P. Cawley, Guided wave health monitoring of complex structures by sparse array systems: influence of temperature changes on performance, *J. Sound Vib.* 329 (12) (2010) 2306–2322.
- [74] A.J. Croxford, et al., Efficient temperature compensation strategies for guided wave structural health monitoring, *Ultrasonics* 50 (4) (2010) 517–528.
- [75] Y. Lu, J.E. Michaels, A methodology for structural health monitoring with diffuse ultrasonic waves in the presence of temperature variations, *Ultrasonics* 43 (9) (2005) 717–731.
- [76] F. Lanza di Scalea, S. Salamone, Temperature effects in ultrasonic Lamb wave structural health monitoring systems, *J. Acoust. Soc. Am.* 124 (1) (2008) 161–174.
- [77] A. Raghavan, C.E. Cesnik, Effects of elevated temperature on guided-wave structural health monitoring, *J. Intell. Mater. Syst. Struct.* 19 (12) (2008) 1383–1398.
- [78] S. Roy, et al., A novel physics-based temperature compensation model for structural health monitoring using ultrasonic guided waves, *Struct. Health Monit.* 13 (3) (2014) 321–342.
- [79] S. Roy, P. Ladpli, F.-K. Chang, Load monitoring and compensation strategies for guided-waves based structural health monitoring using piezoelectric transducers, *J. Sound Vib.* 351 (2015) 206–220.
- [80] S.G. Mallat, Z. Zhang, Matching pursuits with time-frequency dictionaries, *IEEE Transactions on signal processing* 41 (12) (1993) 3397–3415.
- [81] T. Hastie, R. Tibshirani, *Generalized Additive Models*, (1990) (Wiley Online Library).
- [82] S.N. Wood, mgcv: GAMs and generalized ridge regression for R, *R. News* 1 (2) (2001) 20–25.
- [83] S.N. Wood, Fast stable restricted maximum likelihood and marginal likelihood estimation of semiparametric generalized linear models, *J. Roy. Stat. Soc. B* 73 (1) (2011) 3–36.
- [84] S.N. Wood, Thin plate regression splines, *J. Roy. Stat. Soc. B* 65 (1) (2003) 95–114.
- [85] H. Akaike, *Information Theory and an Extension of the Maximum Likelihood Principle*, Springer, 1998, pp. 199–213 *Selected Papers of Hirotugu Akaike*.
- [86] C. Hu, B.D. Youn, J. Chung, A multiscale framework with extended Kalman filter for lithium-ion battery SOC and capacity estimation, *Appl. Energy* 92 (2012) 694–704.
- [87] H. Rahimi-Eichi, F. Baronti, M.-Y. Chow, Online adaptive parameter identification and state-of-charge coestimation for lithium-polymer battery cells, *IEEE Trans. Ind. Electron.* 61 (4) (2014) 2053–2061.
- [88] V. Janapati, et al., Damage detection sensitivity characterization of acousto-ultrasound-based structural health monitoring techniques, *Struct. Health Monit.* 15 (2) (2016) 143–161.
- [89] P. Ladpli, R. Nardari, R. Rewari, H. Liu, M. Slater, K. Kepler, Y. Wang, F. Kopsaftopoulos, F.-K. Chang, Multifunctional energy storage composites: Design, fabrication, and experimental characterization, *ASME 2016 10th International Conference on Energy Sustainability Collocated with the ASME 2016 Power Conference and the ASME 2016 14th International Conference on Fuel Cell Science, Engineering and Technology*, American Society of Mechanical Engineers, 2016pp. V002T01A004.
- [90] P. Ladpli, R. Nardari, R. Rewari, H. Liu, M. Slater, K. Kepler, Y. Wang, F. Kopsaftopoulos, F.-K. Chang, Multifunctional energy storage composites–electrochemical and mechanical cycling characterization, *Proceedings of Battery Congress 2016* (Proceedings vol. 82), Global Automotive Management Council, 2016, pp. 20–33.